Journal of Structural Geology xxx (xxxx) 105388

Contents lists available at ScienceDirect

Journal of Structural Geology

journal homepage: www.elsevier.com/locate/jsg

The 3D model and growth pattern of the Longquan Shan fault zone in Sichuan basin, China: Implications for the potential earthquake rupture patterns

Fang Xu [a,b], Renqi Lu [a,*], Peng Su [a,c], Yann Klinger [b], Jinyu Zhang [a], Yiduo Liu [d], Guanshen Liu [a]

[a] *State Key Laboratory of Earthquake Dynamics, Institute of Geology, China Earthquake Administration, Beijing, China*

[b] *Universite Paris Cite, Institut Physique du Globe de Paris, CNRS, Paris, France*

[c] *Shanxi Taiyuan Continental Rift Dynamics National Observation and Research Station, Taiyuan, China*

[d] *Key Laboratory of Mountain Hazards and Surface Processes, Institute of Mountain Hazards and Environment, Chinese Academy of Sciences, Chengdu, China*

ARTICLE INFO

Keywords:
Longquan Shan fault zone
Fault growth pattern
3D fault model
Seismic interpretation
Fault scaling relationship

ABSTRACT

The fault three-dimensional (3D) structure and growth pattern are fundamental features of an active fault, which provide basic parameters for seismic hazard analysis. The Longquan Shan Fault Zone (LQFZ) is a major active fault, stretching for 200 km in the Sichuan Basin, southwestern China. In this study, we obtain a new, detailed 3D structure model of the LQFZ based on 43 high-resolution seismic reflection profiles. We further quantify the fault heave distribution along the entire LQFZ to understand its growth pattern. We find that the LQFZ contains four major thrust faults and a shallow detachment layer. We obtain 106 displacement values from the seismic profiles and 1963 heave values from the 3D structure model. The heave distribution of the LQFZ contains multiple peaks, indicating that the LQFZ is formed through the linkage of multiple fault segments. The cumulative heave profile of the four faults seems like an isolation fault, which implies the LQFZ has grown coherently since its formation. The maximum displacement and fault length of the four thrust faults show a linear scaling relation, suggesting that the faults grow in a self-similar manner. We also analyze the potential earthquakes on the LQFZ based on the 3D fault model and the fault growth pattern.

1. Introduction

The fault growth through increasing its length and displacement is a fundamental process of crustal deformation (e.g., Scholz, 1990; Elliott, 1976; Cowie and Scholz, 1992a; Schultz et al., 2008). Thus, understanding the fault length and displacement distribution of an active fault provides an insight into the fault growth pattern (e.g., Dawers and Anders, 1995; Ellis and Dunlap, 1988; Nicol et al., 2010; Peacock, 2002; Scholz et al., 1993; Willemse et al., 1996; Bergen and Shaw, 2010; S. Wang et al., 2022), which can be further used to analyze the potential for earthquakes on the fault.

Three fault growth models are always invoked to characterize a fault's growth pattern, i.e., propagating fault model, constant length model, and fault linkage model (e.g., Kim et al., 2000; Nicol et al., 2020a; Walsh et al., 2002): (1) The propagating fault model requires a fault to grow isolated and its displacement and length to grow concurrently (Childs et al., 1995; Walsh et al., 2003; Ze and Alves, 2016, 2017). (2) The constant length model delineates a fault rapidly growing to its final length at the early stage and subsequently remains a constant length as the displacement accumulates (Walsh et al., 2002; Cartwright et al., 1995; Jackson and Rotevatn, 2013; Rotevatn et al., 2019). (3) The fault linkage model suggests that each fault in the fault zone grows in isolation at the early stage, and its length increases abruptly through fault connection at the later stage (Kim et al., 2000; Kim and Sanderson, 2005; Peacock and Sanderson, 1991). Additionally, faults from a fault array may grow in the "coherent fault model", in which the individual fault's growth represents a portion of the fault array's growth (Walsh et al., 2003; Nicol et al., 2010). Constraining the fault displacement distribution along the fault length allows us to analyze the fault growth pattern (e.g., Childs et al., 2003; Baudon and Cartwright, 2008).

The Longquan Shan ("Shan" means Mountains) Fault Zone (LQFZ) is a large active tectonic thrust belt in the Sichuan Basin, on the eastern margin of the Tibetan Plateau (Fig. 1). Densely distributed industrial seismic reflection profiles have been acquired over the entire LQFZ (Fig. 1b). These data allow us to obtain the 3D geometric structure and the displacement distribution of the LQFZ in detail and to further ana-

This article is part of a special issue entitled: Paul Tapponnier published in Journal of Structural Geology.

* Corresponding author.
E-mail address: lurenqi@163.com (R. Lu).

https://doi.org/10.1016/j.jsg.2025.105388
Received 1 July 2024; Received in revised form 17 February 2025; Accepted 27 February 2025
0191-8141/© 20XX

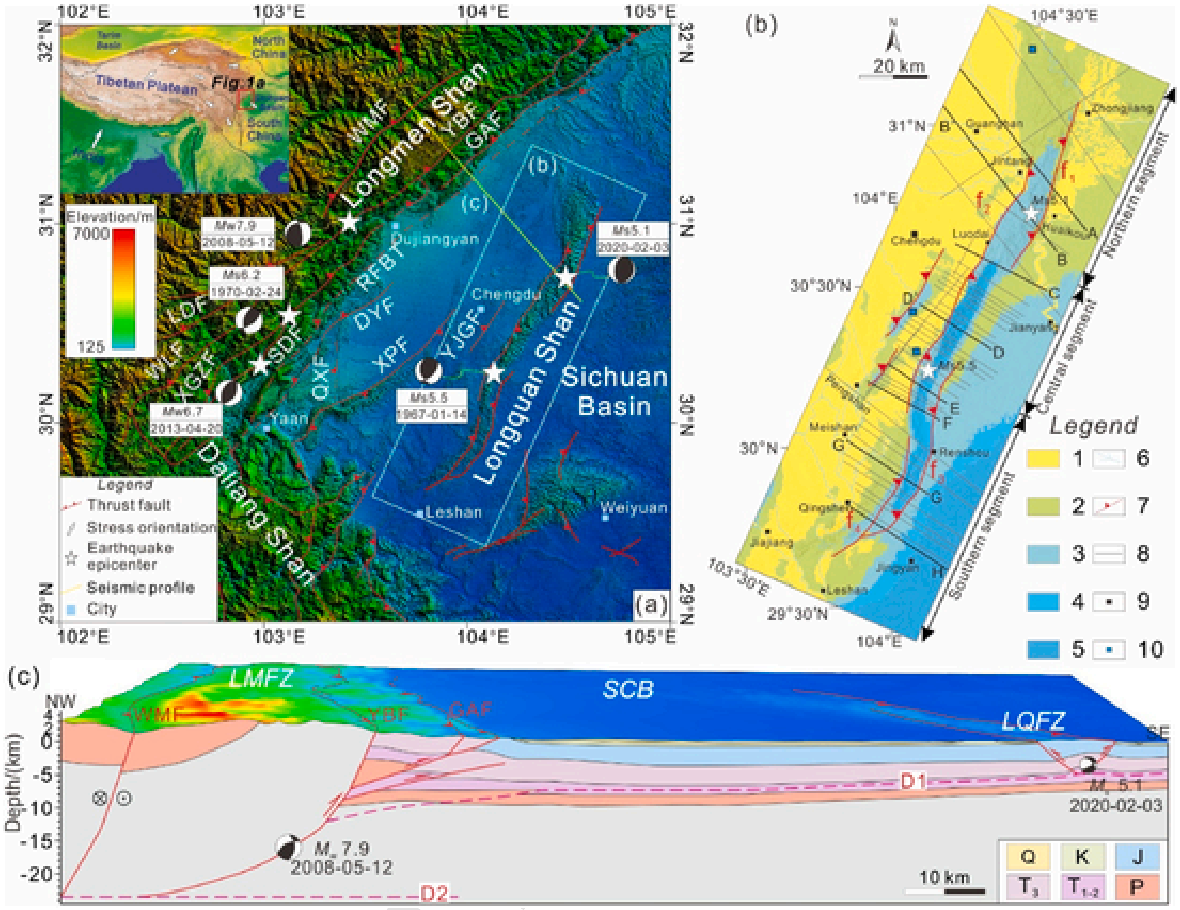

Fig. 1. Topographic and geological map of the Longquan Shan Fault Zone (LQFZ) and its surrounding areas. (a) Regional topographic and neotectonic map of the Sichuan Basin in the eastern margin of the Tibetan Plateau. The Inset map shows the location of Fig. 1a. (b) Geological map of the LQFZ, modified from 1:200000 Sichuan geological maps, including H-48-XX (1971), H-48-9 (1981), H-48-15 (1981), H-48-21 (1981). Black lines denote the locations of the 43 seismic reflection profiles used to construct the 3D structural model of the LQFZ in this study. Bold black lines denote the locations of the seismic profiles A-H that are presented in Figs. 4–7. (c) Oblique topography and the structural cross-section from the southern Longmen Shan Fault Zone to the LQFZ. See the yellow line in Fig. 1a for the section location. Abbreviations: DYF: Dayi fault; GAF: Guanxian-Anxian fault; LDF: Longdong fault; LMFZ: Longmen Shan Fault Zone; QXF: Qiongxi fault; RFBT: Range Front blind thrust; SDF: Shuangshi-Dachuan fault; SSCF: Sansuchang fault; WLF: Wulong fault; WMF: Wenchuan-Maowen fault; XGZF: Xiaoguanzi fault; XKDF: Xinkaidian fault; XPF: Xiongpo fault; YBF: Yingxiu-Beichuan fault; YJGF: Yanjinggou fault. Legends: 1: Cenozoic; 2. Cretaceous; 3: Upper Jurassic; 4: Middle Jurassic; 5: Lower Jurassic; 6: Drainage system; 7: Thrust fault; 8: Location of seismic reflection profiles; 9: City; 10: Well; Q: Quaternary; K: Cretaceous; J: Jurassic; T3: Upper Triassic; T1-2: Middle-Lower Triassic; P: Permian. (For interpretation of the references to color in this figure legend, the reader is referred to the Web version of this article.)

lyze the growth pattern of the thrusting fault zone. Moreover, the LQFZ is close to (~30 km away) the highly populated Chengdu City and is located east of the Longmen Shan Fault Zone (LMFZ), which hosted the devastating 2008 M_w 7.9 Wenchuan earthquake (Fig. 1a) (D. Jia et al., 2010; Xu et al., 2009). The 2008 M_w 7.9 Wenchuan earthquake significantly increased the Coulomb stress in the LQFZ region (K. Jia, 2021; Liu-Zeng et al., 2009; Qian and Han, 2011). Thus, understanding the fault growth pattern of the LQFZ will help to analyze its potential seismic hazard.

Previous studies have preliminarily characterized the fault geometry of LQFZ with the help of two-dimensional industrial seismic reflection profiles: the northern segment consists of two thrust faults with opposite dips, but its geometry was regarded to be a Y-shape by Z. Li et al. (2018) and a herringbone shape by W. Wang et al. (2008); the central segment was regarded as a structural wedge consisting of a SE-dipping thrust fault rooted in the detachment layer (Lu et al., 2010; M. Wang et al., 2016); the southern segment was considered to consist of either two fore-thrust faults and a back-thrust fault (Z. Li et al., 2013) or a fore-thrust fault (W. Wang et al., 2008). There is still some debate regarding the geometry of this fault zone. Furthermore, there is currently a lack of research on the fault growth of the LQFZ.

In this study, we build a new, detailed 3D structural model of the LQFZ using 43 seismic reflection profiles. We further obtained the heave distribution along the fault zone, aiming to identify the different fault sub-segments, the location of inter-segments, as well as the growth and linkage history of the LQFZ. We then analyze the relationship between the maximum displacement and length of the LQFZ and compare our results for the LQFZ with the global thrust fault dataset and the theoretical models to understand its growth history. The subsurface 3D structural characteristics, combined with the analysis of the fault growth pattern and fault segmentation of the LQFZ, provide a new insight into the potential seismic hazards in this area.

2. Tectonic setting

The LQFZ is a prominent fault zone in the Sichuan Basin, which has been regarded as the deformation front of the central and southern LMFZ on the eastern margin of the Tibetan Plateau (Fig. 1a) (Hubbard et al., 2010; Z. Li et al., 2019; Richardson et al., 2008; Tapponnier and Molnar, 1977; C. Wang et al., 2014). The LMFZ contains numerous Mesozoic and Cenozoic thrust faults and nappes (Z. Chen et al., 2005; Luo, 1991; Lu et al., 2014). Pre-Cambrian rocks are involved in the Cenozoic deformation of the LMFZ (D. Jia et al., 2010). The Sichuan Basin is a superimposed basin developed on the western Upper Yangtze Craton and has experienced multi-stage tectonic evolutions (He et al., 2011; Tapponnier et al., 2001; Z. Li et al., 2019). The Sichuan Basin contains multiple detachment layers (Fig. 1c) (L. Tang et al., 2008). The compressional deformation is transmitted from the LMFZ to the Sichuan Basin on the detachment layers (D. Jia et al., 2010; Hubbard et al., 2010; Yan et al., 2011; Y. Liu et al., 2020), resulting in a series of foreland fold-and-thrust belts, such as the Dayi Fault, Xiongpo Fault, and LQFZ (Fig. 1a and c) (S. Liu et al., 1995, 2009). The LQFZ separates the Sichuan Basin into the large deformation domain in the west and the relatively stable area in the east (Fig. 1a) (S. Chen et al., 1994; Deng et al., 1994). The eastern Sichuan Basin has had little to no upper crustal shortening since the late Miocene (Z. Li et al., 2019).

The LQFZ consists of a series of folds and thrust faults, with a total length of ~200 km and a width of ~15–20 km, striking NNE (Fig. 1). W. Wang et al. (2008) separated the LQFZ into three segments mainly based on its surface geometry (Fig. 1b). The western and eastern fault branches bound the Longquan Shan anticline (S. Xu et al., 2006b) (Fig. 1c). The period of formation of the LQFZ is still under dispute, but most believe it occurred during the Quaternary or the Oligocene-Miocene (Richardson et al., 2008; Z. Li et al., 2011). In the LQFZ area, the Pre-Proterozoic basement is capped by Proterozoic-Middle Triassic (or early Late Triassic) marine sediments, which are further overlain by Triassic-Quaternary terrestrial sediments (He et al., 2011; S. Liu et al., 2021; Su et al., 2020). Quaternary, Cretaceous, Jurassic, Triassic, Permian, Cambrian, and Sinian strata are exposed in the LQFZ. Neogene, Paleogene, Carboniferous, Devonian, Silurian, and Ordovician strata are absent in this area. The Permian and Cambrian are in disconformity contact (Fig. 2). Five mechanically weak detachment layers exist in the western Sichuan Basin, i.e., the Middle Jurassic shale detachment layer, the Upper Triassic Coal detachment layer, the gypsum salt detachment layer of the Middle-Lower Triassic, the Cambrian shale detachment layer, and the Precambrian basement detachment layer (Z. Chen et al., 2020; L. Tang et al., 2008), which facilitate the upper crustal deformation in this area. Among them, the Middle-Lower Triassic detachment layer is the main structure that controls the deformation of the Longquan anticline (Z. Li et al., 2013).

3. Data and methods

3.1. Constraining 2D structural cross-sections

We first interpret the 2D structural cross-sections along the LQFZ using 43 well-imaged seismic profiles, which record the structural and stratigraphic information from the near surface to an approximate depth of 8 km. We use two marker horizons to analyze the fault growth, i.e., the bottoms of the Upper Triassic and the Jurassic. We adopt an average velocity of 4000 m s^{-1} for time-depth conversion based on the 3D velocity model of the Sichuan Basin (two-way travel time * average velocity/2) (M. Wang et al., 2016), which is derived from 1166 oil wells, more than 600 seismic reflection profiles, 14 industrial isopach maps, and topographic data. The geological constraints include 1:200,000 geological maps and stratigraphic columns from 3 wells in the Longquan Shan area. Stratigraphic interpretations are constrained by seismic-reflection characteristics and regional interpretations (Z. Li et al., 2013, 2018; Lu et al., 2010; M. Wang et al., 2014; W. Wang et al., 2008). The seismic profile interpretation technique is based on the fault-related fold theory (J. Shaw et al., 2005; Suppe, 1983).

3.2. Building 3D structural model

We then build the 3D structural model of the LQFZ based on the obtained 2D cross sections. The 3D model is established using the SKUA-GOCAD platform. To create the 3D surfaces of the stratum interfaces and faults, we use the "structure & stratigraphy" module based on the discrete smooth interpolation (DSI) technique (Mallet, 1989, 1992; Lévy and Mallet, 1999; Caumon et al., 2009). We finally obtain the 3D stratum interfaces and faults of the LQFZ, which allow us to quantify the fault displacements along the faults.

3.3. Fault heave measurement

To analyze the growth pattern of the faults, we measure the kinematic parameter of the fault heave value (Fig. 3) as the longitudinal stretching of the seismic profiles caused by the time-depth conversion does not affect the horizontal component of the displacement. The Upper Triassic and Jurassic strata are two characteristic formations in the Longquan Shan region, with their basal interfaces displaying distinct reflections in seismic profiles. Additionally, drilling data in the region have strictly calibrated the depths of these two strata. This allows us to accurately depict their geometric shapes, thereby minimizing errors in our measurements of heave and displacement. Consequently, we measured the fault heave values of these two key markers from each constrained 2D structural cross-section and the 3D model of the LQFZ. For some seismic profiles angled at α to the fault strike, we project the measured values to the direction perpendicular to the fault strike (Fig. 3b). Measurements from the 3D model are taken at 200-m intervals along the fault to obtain the detailed fault heave distribution along the entire fault zone.

4. 2D structure of the LQFZ

Previous works show that there are some controversies regarding the fault geometry of this fault zone. Therefore, we constrained the structural styles of different segments of the fault zone, as defined by W. Wang et al. (2008), by interpreting multiple seismic reflection profiles. Three representative seismic profiles were selected for demonstration here.

4.1. Northern segment of the LQFZ

Seismic profile B-B′ shows the general structures of the northern LQFZ (Figs. 1b and 4 and S1a). The Longquan Shan anticline in this segment shows symmetrical geometry. The Jurassic strata are exposed in the core of the anticline. The residual Cretaceous strata crop out on both limbs of the anticline. The Quaternary is only presented on its western limb. The Permian strata and Cambrian strata are in disconformity contact. The Triassic and Jurassic strata progressively thin southeastward, whereas the thicknesses of the Permian and Cambrian strata are nearly constant (Fig. 4).

In the eastern limb of the anticline, there exists a relatively poorly imaged area at 0–5 km depth, the strata on both sides of this area have obviously different burial depths, with a displacement of about 700 m. We thus interpret this area as the eastern branch fault f_1 of the LQFZ. The fault f_1 roots into the Middle-Lower Triassic gypsum and salt detachment layer, cutting through the Middle-Upper Triassic, Jurassic, and Cretaceous units. Under the western limb of the anticline, the discontinuous reflection wave group indicates the location of the western fault branch f_2 of the LQFZ, with a cumulative displacement of ca. 800 m. The seismic profile clearly images the interface of the Triassic strata. The Upper Triassic T_3 and the upper part of the Middle-Lower Triassic $T_{1\text{-}2}$, are offseted by the fault f_2.

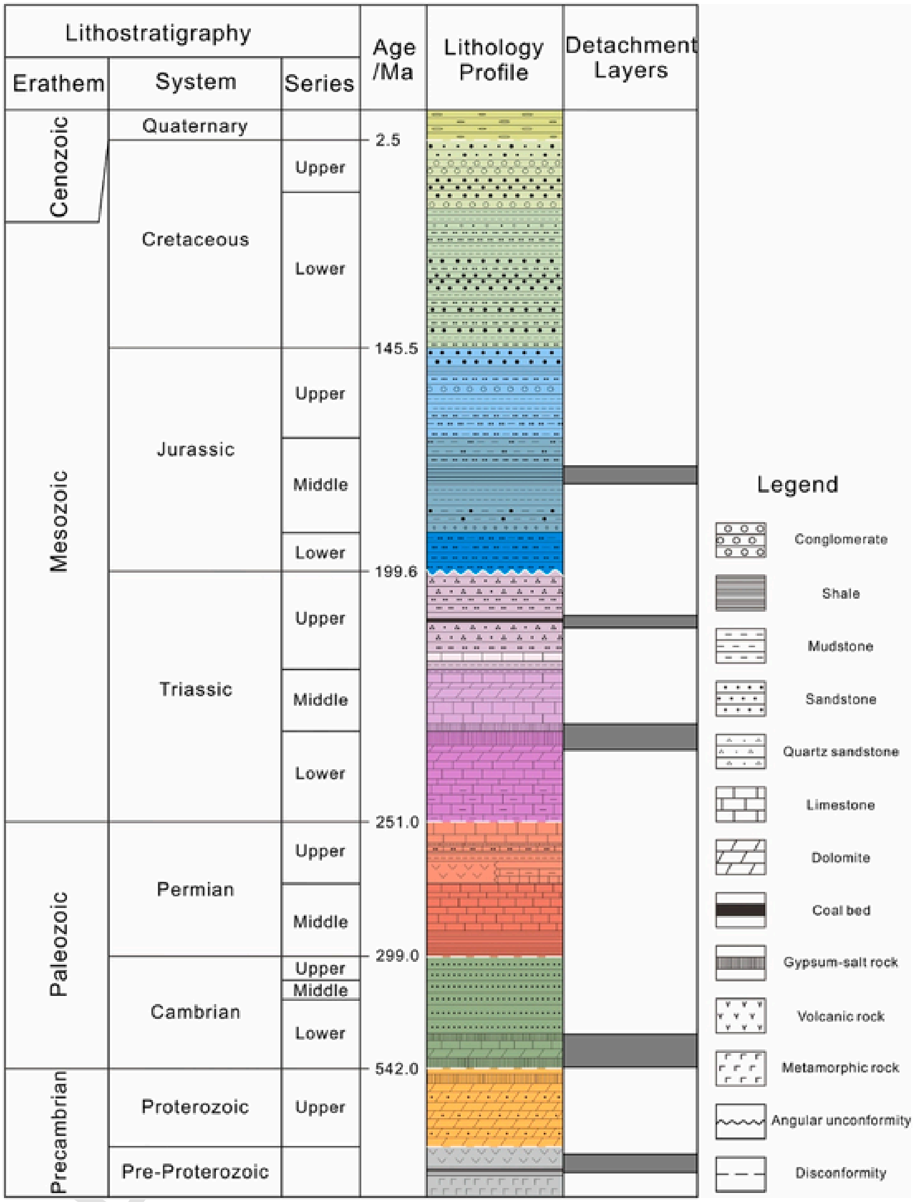

Fig. 2. Stratigraphic column in the Longquan Shan area (Modified from 1:200000 Sichuan geological maps, including H-48-XX (1971), H-48-9 (1981), H-48-15 (1981), H-48-21 (1981)).

4.2. Central segment of the LQFZ

Profiles D-D′ represents the structures in the central LQFZ (Figs. 1c and 5 and S1b). The Longquan Shan anticline on this profile shows an asymmetric morphology, with a wide, gentle western limb and a narrow, steep eastern limb (Fig. 5). Stratigraphy along this profile is similar to that along the profile B-B′ to the north, but the overall burial depth becomes shallower. The Triassic strata also show a characteristic wedge shape, i.e., thicker in the west and thinner in the east, but the degree of thinning is smaller than that of the profile B-B'.

The fault plane reflection and the offset of the in-phase axis indicate the location of the SE-dipping thrust fault f_2, whose cumulative displacement is ca. 2300 m (Fig. 5). The fault f_2 cuts the Cretaceous, Jurassic, and Middle-Upper Triassic, and then soles into the detachment in the Middle-Upper Triassic.

The fault f_2 connects the detachment, forming a wedge-shaped fault block in the footwall of f_2 (Fig. 5). The movement of the wedge-shaped fault block causes folding deformation in the hanging wall of the fault f_2. The position of the wedge tip is concordant with the intersection of the eastern synclinal axial plane and the detachment. Furthermore, the fault f_2 is largely planar in this section, and the strata in its kink bands are nearly parallel to the fault. This geometric pattern suggests that the LQFZ in this segment is controlled by the classic fault-bend fold-structural wedge (J. Shaw et al., 2005; Suppe, 1983) (Fig. 5b). Our interpretation of the "structural wedge" fold of this segment is consistent with the interpretation by Lu et al. (2010) and M. Wang et al. (2022).

4.3. Southern segment of the LQFZ

The key structural characteristics in the southern LQFZ can be represented by the seismic profile G-G' (Figs. 1c and 6 and S1c). The stratigraphic framework of the profile G-G' (Fig. 6) is largely identical to that of the northern and central segments (Figs. 4 and 5).

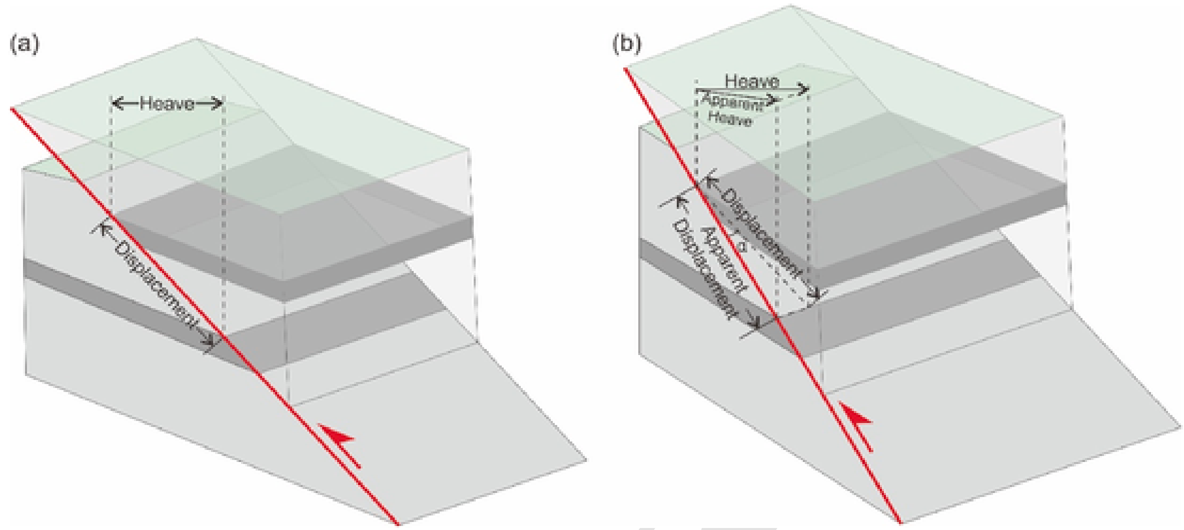

Fig. 3. Diagrams show the fault heave and displacement measured in this study. Heave and displacement measurement on the profile perpendicular(a) or oblique(b) to the fault strike. α is the angle between the two sections that are perpendicular and oblique to the fault strike respectively.

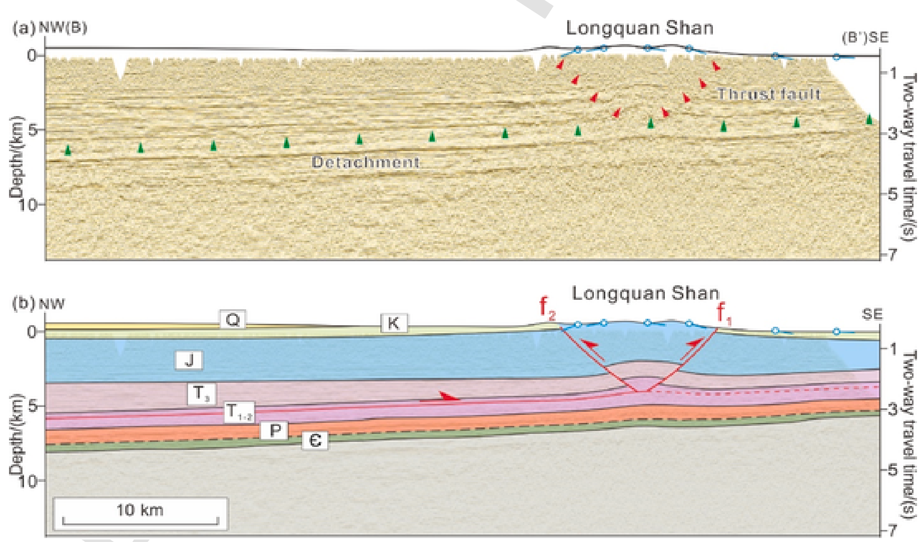

Fig. 4. Seismic profile B-B′ across the northern segment of the LQFZ. (a) Uninterpreted seismic profile. The red triangles mark the locations of the thrust faults, and the green triangles mark the detachment location. (b) Interpreted seismic profile. The dashed red line denotes the detachment layer, and the dashed black line denotes the disconformity contact. Abbreviations: Q: Quaternary; K: Cretaceous; J: Jurassic; T_3: Upper Triassic; $T_{1\text{-}2}$: Middle-Lower Triassic; P: Permian; Є: Cambrian. (For interpretation of the references to color in this figure legend, the reader is referred to the Web version of this article.)

The change of the dip and depth of the Upper Triassic and Jurassic strata in the Longquan Shan anticline indicates the presence of an NW-dipping thrust fault (i.e., f_3) beneath the eastern limb of the anticline (Fig. 6). The fault f_3 has a cumulative displacement of ca. 1800 m. It originates from the detachment layer and cuts the overlying Upper Triassic and Jurassic strata, which is characterized by the breakthrough of the fault-propagation fold (J. Shaw et al., 2005; Suppe, 1983) (Fig. 6b). We also interpret a minor synthetic fault f_4 in the Jurassic strata in the western limb. The back-thrust fault that was suggested by Z. Li et al. (2013) cannot be identified on any seismic profiles in this area, and based on our interpretation, only two faults f_3 and f_4 exist in the southern segment.

5. 3D structural model of the LQFZ

We interpret 43 seismic profiles and construct the 3D structural model of the LQFZ (Figs. 7 and 8, and Supplementary Movie S1). Overall, the LQFZ comprises the four major faults f_1-f_4.

Supplementary video related to this article can be found at https://doi.org/10.1016/j.jsg.2025.105388

The north part of the LQFZ is dominated by the pop-up structure defined by the two opposite-dipping thrust faults f_1 and f_2 (Figs. 4, 7A and 7B, and 8). Both faults sole into the Middle-Lower Triassic detachment. The fault f_2 terminates near Jintang County, and the fault f_1, a NW-dipping thrust fault, extends further to the north (Figs. 1c–8). Southward, the SE-dipping thrust fault f_2 extends and forms a "structural wedge" with the detachment layer (Figs. 5, 7C and 7D, and 8). The NW-dipping thrust fault f_3 is present in the south. The f_3 gradually deepens

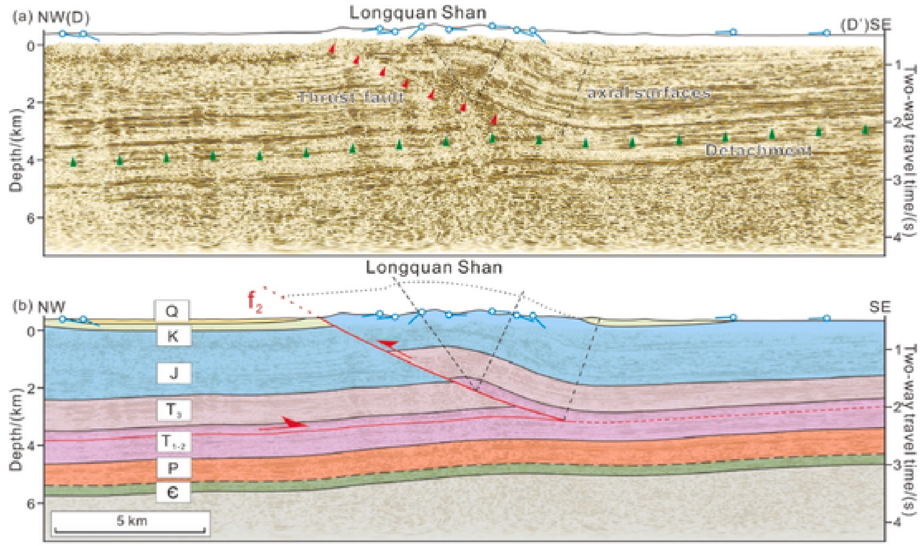

Fig. 5. Seismic profile D-D′ across the central segment of the LQFZ. (a) Uninterpreted seismic profile. (b) Interpreted seismic profile. The dotted black curve represents the eroded contact between the Jurassic and Cretaceous. Refer to Fig. 4 for the marker descriptions and the abbreviations.

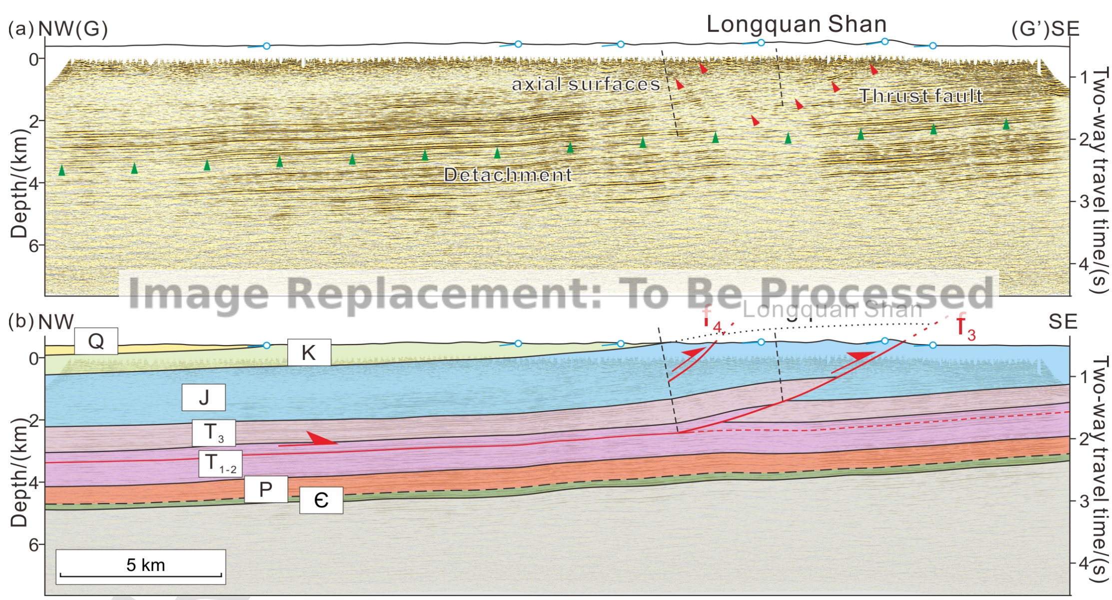

Fig. 6. Seismic profile G-G′ across the southern segment of the LQFZ. (a) Uninterpreted seismic profile; (b) Interpreted seismic profile. Refer to Figs. 4 and 5 for the marker descriptions and the abbreviations.

southward, which connects the SE-dipping thrust fault f_2 in its northern portion and soles into the Middle-Lower Triassic detachment in its middle and southern portions (Fig. 7E and F, and 8). Further to the south, the NW-dipping thrust faults f_4 appears, which gradually deepens southward and finally soles into the Middle-Lower Triassic detachment (Figs. 6, 7G and 7H, and 8). The faults f_3 and f_4 extend a short distance further south (Fig. 1b), but we do not have data to constrain their structures.

The 3D model shows that faults f_1 and f_4 are nearly planar with relatively uniform dips of 40°~60° and 20°~30°, respectively (Fig. 8a). In contrast, the faults f_2 and f_3 are non-planar. The fault f_2's dip angles increase southward. The fault f_3 has a S-shaped surface trace and can be divided into two parts. The southern part is listric with gentle dips up to ~25°, whereas the northern part is relatively planar with larger dips of 50°~60°.

The detachment shallows southeastward in the Longquan Shan region, which is ~5.8 km in depth near Qingbaijiang and ~1.8 km to the east of Leshan (Fig. 8). Such a systematic variation is consistent with the thickness variation of the detachment-bearing Middle-Lower Triassic strata (Figs. 4–7).

6. Fault heave distribution of the LQFZ

The fault heave distribution profiles allow us to analyze the growth patterns of each fault and the whole LQFZ (Fig. 9) (Song et al., 2019; Totake et al., 2018). The fault heave value distribution obtained from the 3D model is highly consistent with that measured from the seismic

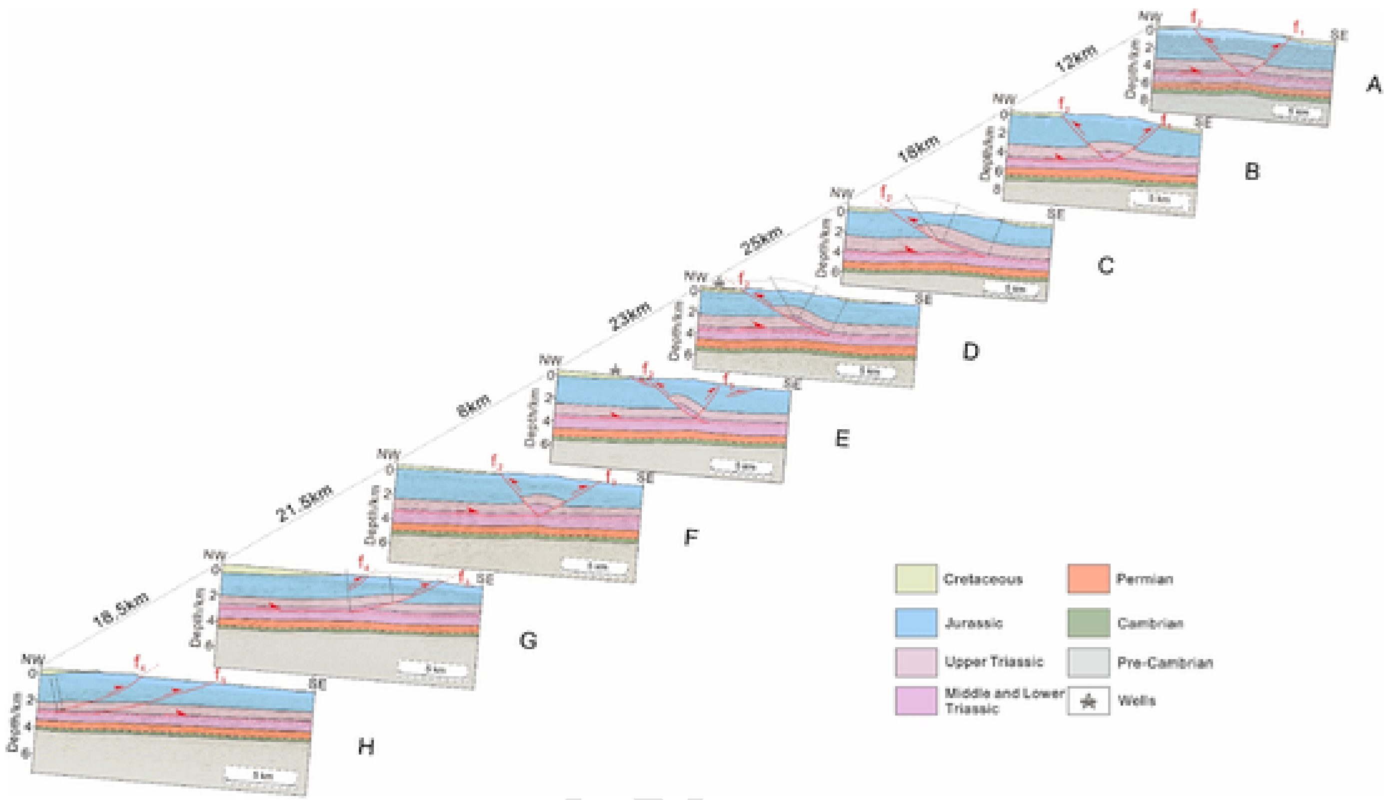

Fig. 7. The representative interpreted seismic profiles (A–H) that are used to construct the 3D model of the LQFZ. The location of A-H is shown in Fig. 1c.

reflection profiles, despite the DSI interpolation method prioritizing the preservation of overall surface continuity over precisely matching each original data point (Fig. 9). The fault heave distribution profiles have multiple peaks and exhibit an asymmetrical feature. These peaks correspond to the nucleation sites of the main fault segments, and the troughs reflect the linkage regions between the adjacent fault sub-segments (Davis et al., 2005; Nicol et al., 2010; Peacock and Sanderson, 1991; Soliva and Benedicto, 2004; Ferrill et al., 2016). This fault heave distribution pattern indicates that each of the four faults f_1-f_4 in the LQFZ is formed via the linkage of fault sub-segments. Moreover, the larger the heave value at the linkage zone, the earlier the linkage may have started (S. Wang et al., 2022). Therefore, the fault heave distribution profile may also imply the linkage process among fault sub-segments (Bergen and Shaw, 2010). Secondary peaks can be seen at the fault heave distribution profiles of the faults $f_{3\text{-}1}$, $f_{3\text{-}2}$, $f_{2\text{-}2}$, and $f_{2\text{-}5}$, indicating the presence of more secondary fault segments.

Existing data of fault f_1 show that the maximum heave value is about 0.6 km, and no obvious trough has been identified (Fig. 9b). We simply speculate that the growth of fault f_1 did not involve linkage between sub-segments. Fault f_4 is the shortest in the LQFZ, and the heave value of the limited seismic profiles and the model heave curve still shows obvious fluctuations (Fig. 9e). We infer that this fault consists of at least three fault segments, with the third fault sub-segment to the south not being constrained by seismic reflection profiles and possibly-being longer. The identifiable highest peak of the Jurassic marker can reach ~450 m, and the lowest trough is ~120 m (Fig. 9e). Seismic reflection profiles are sparsely distributed for these two faults, and thus they will not be discuss further in this work.

Six prominent heave peaks can be recognized along the fault f_2's heave distribution profile (Fig. 9c). This suggests that the fault f_2 was formed via the linkage of at least six fault sub-segments. The highest peak in the heave distribution profile constrained by the Upper Triassic marker reaches ~3.5 km, whereas the lowest trough shows a heave value of ~0.3 km. The smallest heave distribution gradient along the fault is between sub-segments $f_{2\text{-}1}$ and $f_{2\text{-}2}$. These two sub-segments may be more tightly linked compared to the other sub-segments being part of this fault.

Similar to the f_2, the fault f_3 has at least four peaks in its heave distribution profile (Fig. 9d), indicating at least four fault sub-segments. The highest peak of the fault heave distribution constrained by the Upper Triassic marker reaches up to ~2.3 km, whereas the lowest trough is ~0.1 km (Fig. 9d). A large heave gradient exists between each heave peak and trough and the deficit at each heave trough indicates that the fault is in the early stage of linkage and the intersegment that has not yet received heave compensation.

7. Discussion

7.1. The growth pattern of the LQFZ

The heave profiles of the four faults in LQFZ mostly presents a multi-peak distribution (Fig. 9), which indicates that multiple sub-segments are involved in the fault growth process. The faults, f_2-f_4, are formed by linking 6, 4, and 3 sub-segments respectively. They may have initiated separately, propagated laterally until they overlapped to coalesce, and finally formed a new fault, which has also been observed previously (Ellis and Dunlap, 1988; Walsh et al., 2003; Higgins et al., 2009). After the fault sub-segments linked, the area between the fault sub-segment tips will exibit a deficit in the total heave. Previous studies have shown that the mirror-image relationship between fault heave and fold strains indicates strain transfer between folds and faults (Elliott., 1976; S. Liu and Dixon, 1991; Higgins et al., 2009). We can see that the heave trough often corresponds to a smaller fold interlimb angle which represents a higher fold strain (Fig. S2). Therefore, deformation such as folds and strata rotation in the area of the LQFZ will compensate for the heave

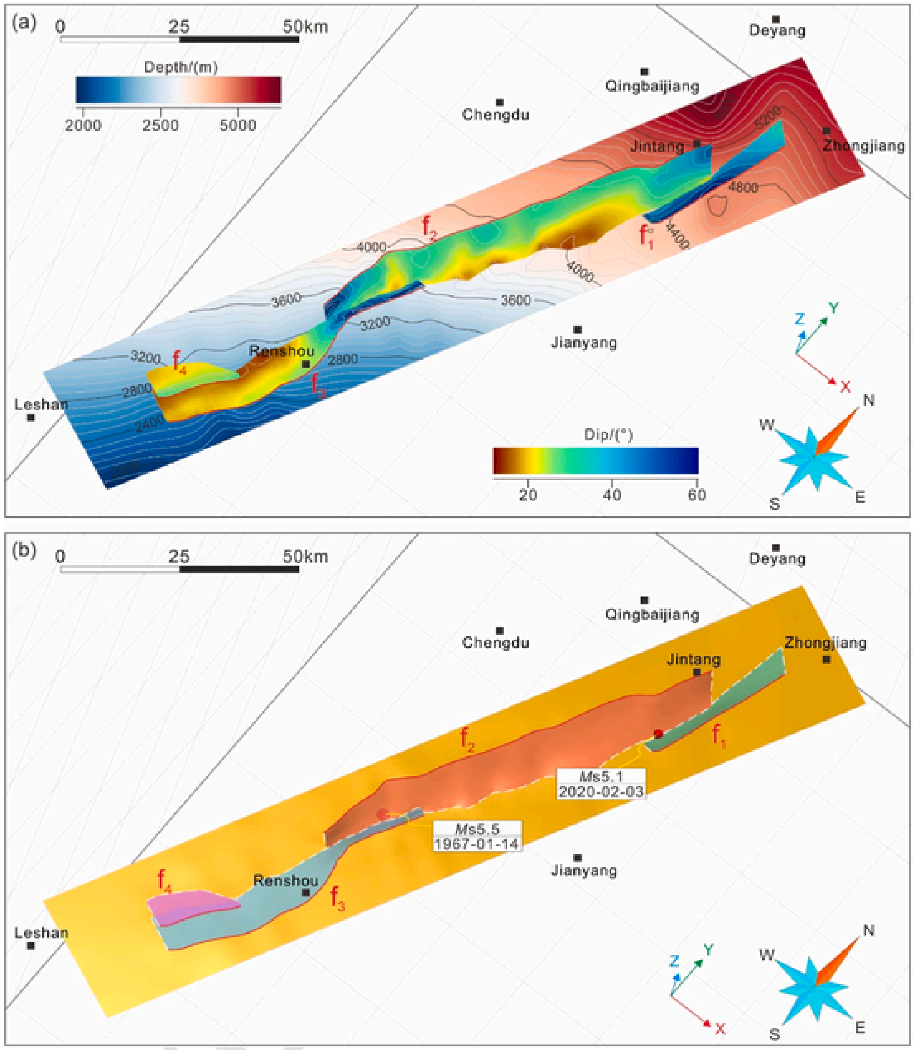

Fig. 8. Three-dimensional display of the LQFZ and the Triassic evaporite detachment. (a) Three-dimensional display of the detachment depth isocline and fault dip isocline in the LQFZ region. (b) Three-dimensional display of the LQFZ with the 2020 Qingbaijiang M_s 5.1 and the 1967 Renshou M_s 5.5 earthquakes. The fault surfaces f_1-f_4 are shown in different colors. The yellow surface denotes the Triassic detachment layer. (For interpretation of the references to color in this figure legend, the reader is referred to the Web version of this article.)

deficit shown in the curve, as also observed in previous work (Nicol et al., 2020a; Totake et al., 2018).

We then normalize each fault's heave distribution profile of the LQFZ on the same graph, and considering the maximum value of Displacement/Length (D/L) is 0.1 (Nicol et al., 2020b), we enlarged the normalized heave value by 100 times and the normalized length value by 1000 times (Fig. 10a and b). Their curves do not follow any single pattern and are quite different from the heave profile of an individual isolated fault which is characterized by smooth and uniform aggregate heave distribution (Bergen and Shaw, 2010; Walsh et al., 2003). We also obtained the total fault heave distributions of the entire LQFZ and similarly normalized and enlarged them (Fig. 10c). The total heave profile is less variable than the heave profiles of the single fault. It shows a relatively smooth and regular total heave distribution, similar to the heave distribution profiles of an individual isolated fault (Walsh et al., 2002). This indicates a significant increase in system stability from a larger spatial scale (Nicol et al., 2010). Also considering that the ratio of (distance between the faults) over (displacement) is less than 10 on the fault zone (Barnett et al., 1987; Childs et al., 2003; Nicol et al., 1996, 2020a; Rippon, 1984), we propose that the four faults of the LQFZ have been kinematically related since the beginning of their formation (Childs et al., 2017) and have jointly accommodated the strain. This growth pattern, characterized by the jointly accommodation of faults to strain and the transfer of strain between faults and folds, is analogous to that observed in the Tibetan Plateau, notable examples include the Altyn fault zone in the northern plateau (Meyer et al., 1998) and the Qiongxi thrust fault system in the Sichuan Basin (Song et al., 2019). Taking the f_2 and f_3 as an example (Fig. 9f), the northern part of f_3 overlaps with the southern part of f_2, and the strain in this area may be preferentially accommodated by fault f_2, thus resulting in a larger heave on f_2 and a smaller heave on f_3. Nevertheless, we cannot rule out the possibility that they may grow in isolation for a short period of their geological history.

High displacement gradients can be observed across the fault boundaries of the LQFZ (Fig. 9). This may be attributed to the tendency for a new fault to increase heave and decrease heave deficit first after fault sub-segment linkage. The occurrence of the next fault lateral propagation will happen when the D_{max}/L ratio reaches the characteristic value of this area (Kim and Sanderson, 2005; Song et al., 2019). Another possible contributing factor is that the interaction between coherent faults/fault sub-segments also leads to the slowdown of lateral propagation of the existing faults, and the length of the faults is basi-

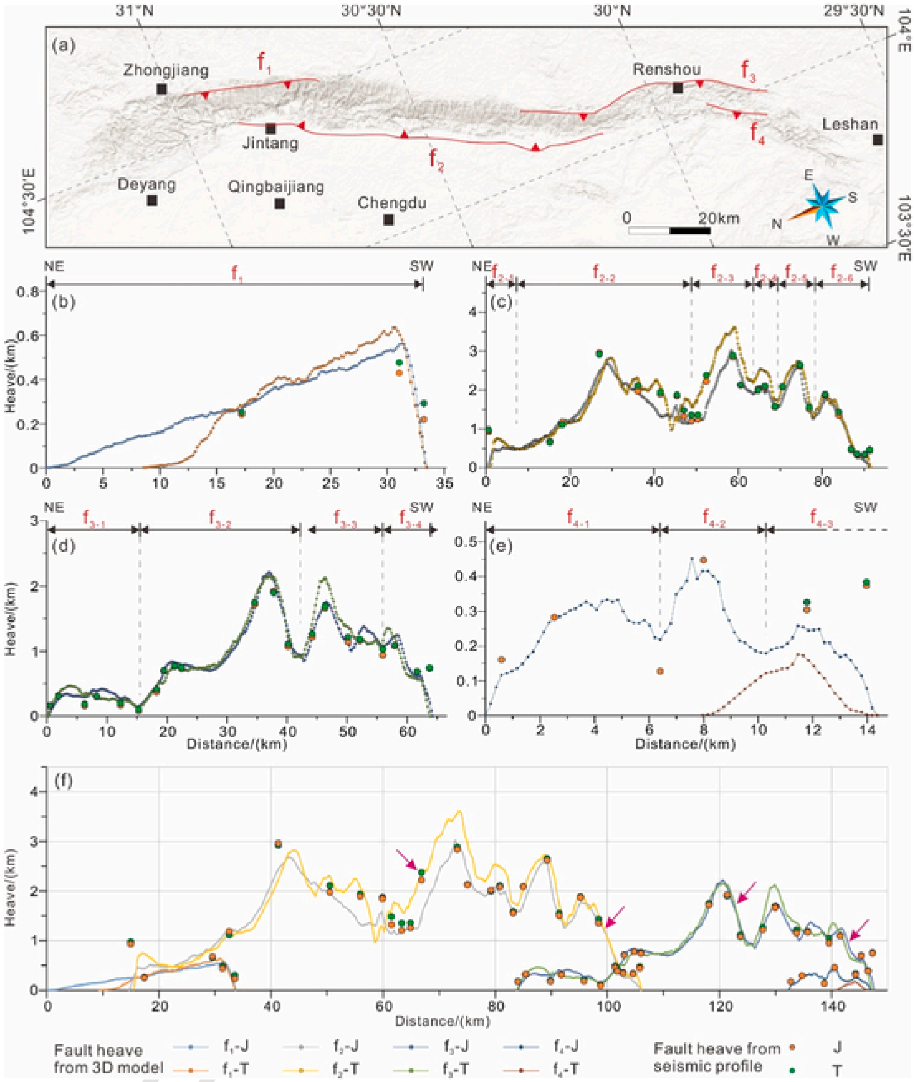

Fig. 9. Fault heave distribution profiles of the LQFZ. (a) Fault surface traces of the LQFZ obtained from the 3D fault model. (b–e) Heave distribution profiles of the faults f_1, f_2, f_3, and f_4. Each fault contains multiple sub-segments. (f) The heave distribution profiles of the entire LQFZ. Purple arrows point out some locations with high heave gradients as examples. The heave values from 3D model used in the figure can be found in Table S1. (For interpretation of the references to color in this figure legend, the reader is referred to the Web version of this article.)

cally unchanged as heave increases (Peacock and Sanderson, 1996; Willemse, 1997; Nixon et al., 2014).

7.2. Scaling relationships between D_{max} and L of the LQFZ

The relationship between the fault maximum displacement (D_{max}) and the fault length (L) has been widely investigated based on a large amount of fault data worldwide (Bailey et al., 2005; Fossen and Hesthammer, 1997; ; Nicol et al., 2017; Schlische et al., 1996). A consensus on this relationship is:

$$D_{max} = cL^n$$

where c, called *scale factor* or *characteristic shear strain*, is a constant related to the material properties of the host rocks and is an expression of the fault displacement per unit length (Bailey et al., 2005; Cowie and Scholz, 1992b; Watterson, 1986; S. Xu et al., 2006a). The index value n ranges from 0.5 to 2, with $n = 1$ indicating that the fault follows a linear scale, i.e., self-similar growth, and $n \neq 1$ indicating a scale-dependent geometry (Cowie and Scholz, 1992c; Fossen and Hesthammer, 1997; Gillespie et al., 1992; Scholz et al., 1993; Walsh and Watterson, 1988).

We plot the eight pairs of the fault maximum displacements and fault lengths of the four faults cutting the Jurassic and Upper Triassic in the LQFZ. Both linear and power-law regressions can describe the D_{max}-L relationship well: the regression yields a best-fit index n of 1.26 and a coefficient of determination (R^2) of 0.98 for the power-law scaling relationship (Fig. 11a). Considering the n and R^2 values are close to 1, we also conduct a linear regression of the observed data (Fig. 11b), which yields a scale factor of 0.03 and an R^2 of 0.97. Since the R^2 value of the two regressions are very close, we thus consider the more simpler one, i.e. linear D_{max}-L theoretical model ($n = 1$ and $D_{max} = cL$), can well characterize the fault growth in the LQFZ, which is characterized by a self-similar growth (Kim and Sanderson, 2005; Meyer et al., 1998; Walsh et al., 2002).

The scaling relationship between D_{max} and L depends on several factors, including but not limited to sampling bias, mechanical properties of the rock, tectonic setting, age of the fault, and fault interactions (Bailey et al., 2005; Cartwright et al., 1995; Dawers and Anders, 1995; Mouslopoulou et al., 2009; Nicol et al., 2010, 2020a; Poulimenos, 2000;

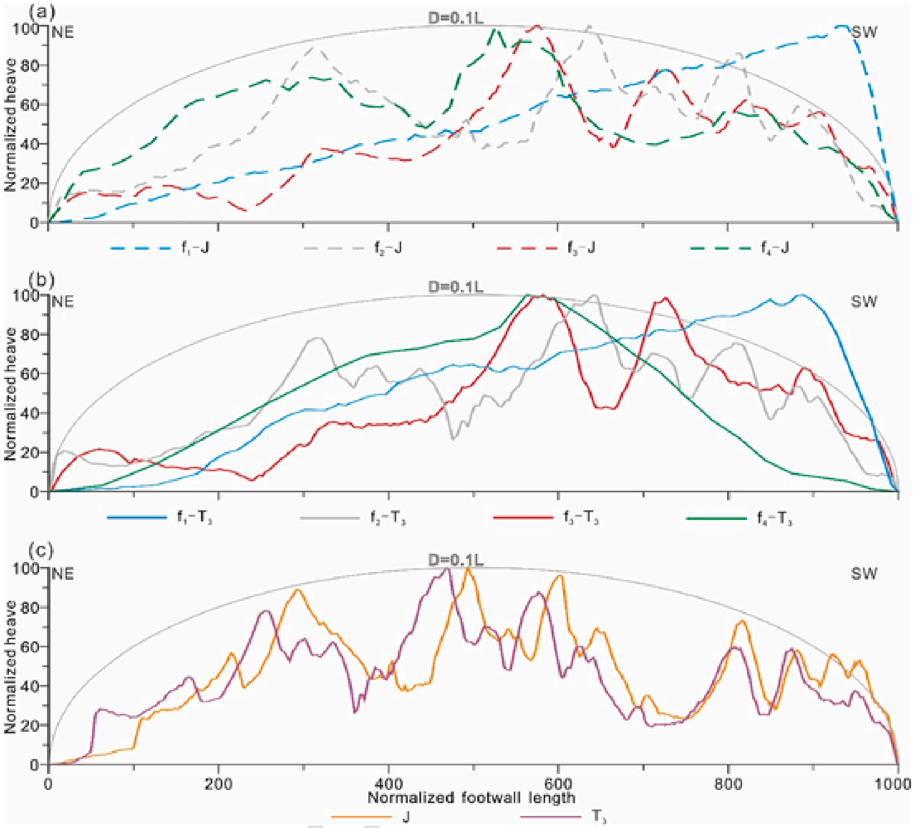

Fig. 10. Normalized displacement distribution profiles of the LQFZ. (a)The fault heave distribution profiles of the faults f_1-f_4 constrained by the Jurassic marker. (b) The fault heave distribution profiles of the faults f_1-f_4 constrained by the upper Triassic marker. (c)Cumulative heave distribution profiles of the entire LQFZ constrained by the Jurassic and the Upper Triassic markers. The gray line represents the smooth and regular total heave distribution profile of an individual isolated fault.

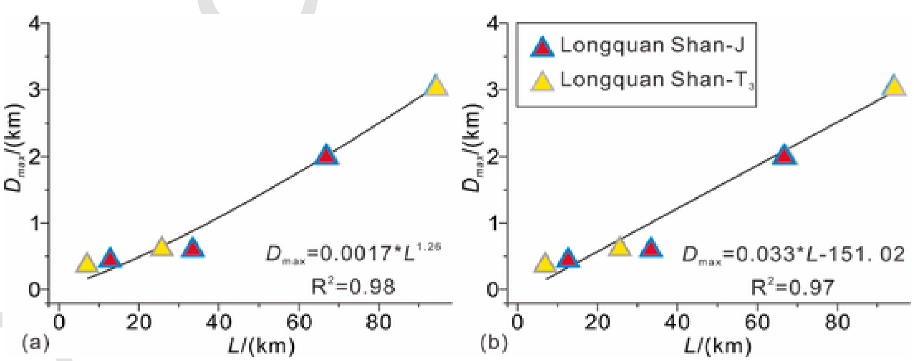

Fig. 11. Maximum fault displacement (D_{max}) versus maximum fault length (L) of fault f_1-f_4 in the LQFZ. (a) Fitting the D_{max} and L data with a power function. (b) Fitting the D_{max} and L with a linear function. The displacement value measured from the seismic profiles can be found in Table S2.

Walsh et al., 2002; Wojtal, 1994). Our data do not show a great scatter, and even fit well with the linear function. Therefore, the influencing factors mentioned above may be less variable over a long geological history period since the formation of the LQFZ. Moreover, the D_{max} and L data of the LQFZ fall in the trend of the global thrust fault data (Fig. 12). This adds new and valuable data to the under-investigated database.

7.3. Potential seismic hazard for the LQFZ

Considering that the LQFZ is seismically active, as it hosted a M_s 5.1 Qingbaijiang earthquakes in 2020 (Lei et al., 2020; F. Xu et al., 2022), and that it is close to the highly populated Chengdu metropolitan area, its seismic hazard deserves evaluation (Fig. 1). We particularly focus on the potential seismic hazard caused by the rupture of the fault f_3 of the LQFZ since $M > 5$ earthquakes have occurred in both the central and northern segments (Huang and Jiang, 2012; S. Xu et al., 2006b).

Most earthquakes either rupture a fault segment or multiple fault segments (DePolo et al., 1991; Machette et al., 1991; Oglesby, 2008;

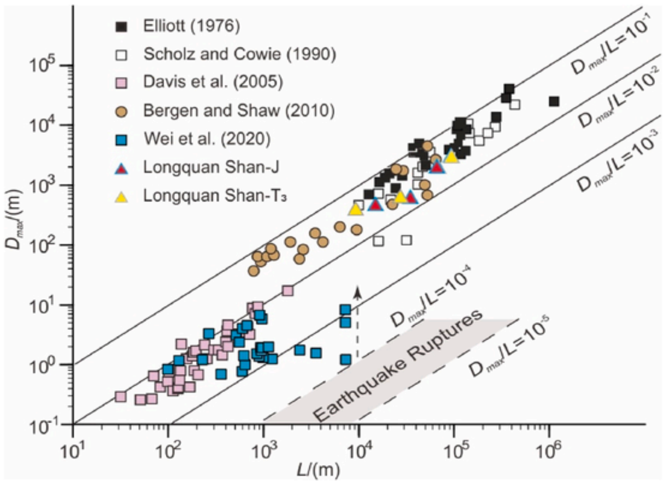

Fig. 12. Plot of maximum displacements versus lengths of thrust faults (modified from Wei et al., 2020 and references therein).

Schwartz and Coppersmith, 1984; Yue et al., 2005; P. Zhang et al., 1991, 1999), or fail in a cascade rupture behavior (Kaneda et al., 2008; Kase, 2010; Oglesby, 2005; B. Shaw and Dieterich, 2007; Wesnousky, 2006; Yu et al., 2010). Active fault's geometric complexity depends on segmentation and partially controls potential earthquake magnitudes (Deng and Wen, 2008; Guyonnet-Benaize et al., 2015; Klinger, 2010; J. Wang et al., 2020). It also affects the earthquake nucleation, dynamic rupture, stress triggering, and seismic wave propagation (Mildon et al., 2019; Ross et al., 2020). The obtained new 3D structural model and the fault growth pattern help to estimate the potential seismic magnitude of the LQFZ.

Fault grows through the superposition of earthquake rupture (Watterson, 1986; Dawers et al., 1993; Walsh et al., 2002; Fossen, 2020). For an active fault that grows in the propagating model or the constant length model, the static stress distribution is usually concentrated at the fault tip (Fig. 13a and b) (Schlagenhauf et al., 2008). For an active fault that ruptures in the fault linkage model, e.g., the LQFZ, the static stress distribution is more non-uniform and concentrated at the edges of fault sub-segments (Fig. 13c) (Manighetti et al., 2007; Wilson et al., 2003). Such areas accommodate strains in a plastic manner and thus act as structural barriers to seismic rupture propagation (Fig. 13c) (Black and Jackson, 2008; Manighetti et al., 2009, 2015). Therefore, the earthquake on the LQFZ may rupture a sub-segment or overcome the structural barrier and cause a greater rupture (Machette et al., 1991; P. Zhang et al., 1991, 1999). In addition, the earthquake on the LQFZ may rupture in a cascading way since the fault surfaces intersect at depth or sole into the detachment layer at a very small distance though some areas present oppositely inclined fault planes (Wesnousky, 2006), like during the 2013 M_w 6.7 Lushan earthquake in the Longmen Shan area of Sichuan (Fig. 1a) (e.g., Lu et al., 2017) or the 1999 M_w7.6 Chichi earthquake in Taiwan (Lee et al., 2002).

We test a hypothetical rupture on fault f_3 (Table S3). When only one fault sub-segment ruptures, the maximum magnitude of the earthquake that can be induced is estimated to be M_w 6.4. When multiple fault sub-segments are ruptured, based on the heave distribution profile of f_3 (Fig. 9d), $f_{3\text{-}1}$ and $f_{3\text{-}2}$ may rupture together considering the small heave gradient between the two sub-segments. In this case, the rupture of the two sub-segments can produce an M_w 6.5 earthquake. Furthermore, cascading ruptures of all four faults of the LQFZ could produce a maximum M_w 7.1 earthquake. Considering the shallow fault depth in the southern segment of the fault zone, and because the empirical formulae are usually based on plate boundaries or intra-continental seismically active orogenic zones (e.g. Henry and Das, 2001; Leonard, 2010; Wells and Coppersmith, 1994), there may be certain biases in the magnitude estimation of intra-basin earthquakes. Therefore, the estimated magnitudes should be used with caution.

8. Conclusions

We interpret 43 seismic reflection profiles across the Longquan Shan fault zone (LQFZ) in the eastern Tibetan Plateau margin and establish a new, detailed 3D fault model of the LQFZ. We have extracted the heave distributions of the four faults based on the model and quantitatively analyzed the fault growth pattern of the LQFZ. We have further assessed the potential earthquake magnitude of the LQFZ by combining the 3D geological model and the fault growth pattern.

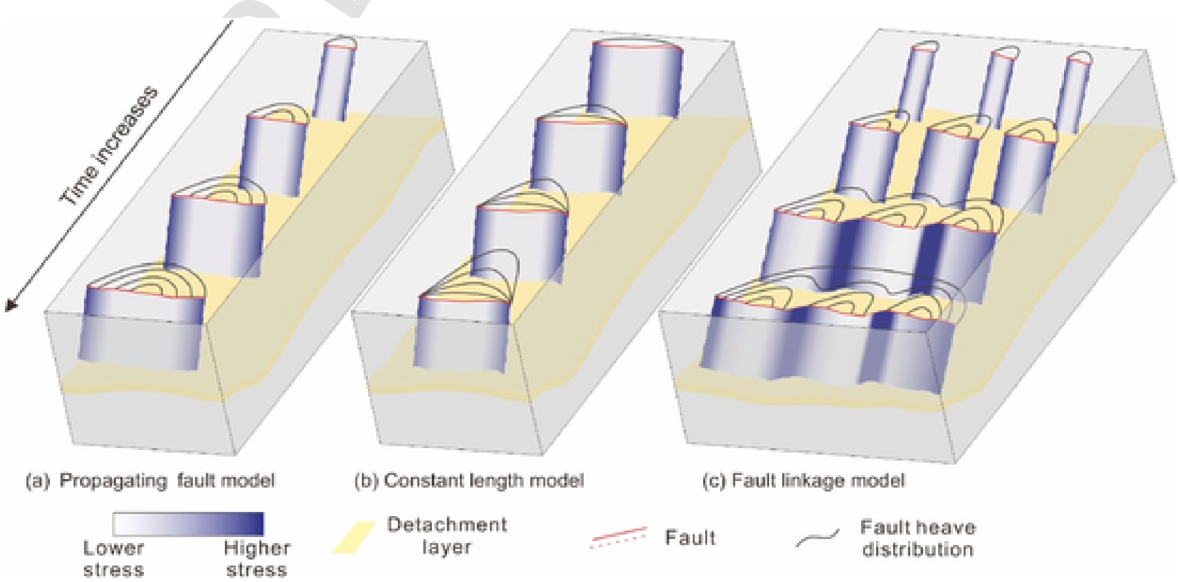

Fig. 13. An active fault rupture model for the three end-member growth models. Modified from Kim and Sanderson (2005), Manighetti et al. (2015) and Schlagenhauf et al. (2008).

(1) The LQFZ contains four major faults, termed f_1-f_4, forming a pop-up structure in the northern, a structural wedge in the central, and a fault-propagation fold in the southern segment of the Longquan Shan. Along-strike variations characterize the geometry of these faults. Faults f_1 and f_4 have relatively uniform dip angles. The dip angle of fault f_2 increases southward, and f_3 exhibits S-shaped characteristics, with the northern dip angle being larger than that of the south part. The detachment layer in this area is about 1.8–5.8 km deep and it deepens southeastward.
(2) Fault f_1-f_4 developed by linking a series of fault sub-segments. The whole fault zone may have been kinematically related since its formation. The maximum displacement (D_{max}) and fault length (L) data of the faults show a linear positive correlation, which is consistent with the trend of the global thrust fault dataset.
(3) Considering the barrier effect of inter-segments on earthquake rupture, we propose that an M_w 6.5 earthquake could occur on the LQFZ when multiple fault sub-segments of fault f_3 are ruptured, and the LQFZ has the potential for strong earthquakes.

CRediT authorship contribution statement

Fang Xu: Writing – original draft, Visualization, Methodology, Investigation, Conceptualization. **Renqi Lu:** Writing – original draft, Visualization, Resources, Methodology, Funding acquisition, Conceptualization. **Peng Su:** Writing – original draft, Visualization, Methodology, Conceptualization. **Yann Klinger:** Writing – review & editing. **Jinyu Zhang:** Writing – review & editing. **Yiduo Liu:** Writing – review & editing. **Guanshen Liu:** Writing – review & editing.

Data availability

The seismic reflection data, drilling wells, and structural maps were provided courtesy of the Southwest Oil and Gas Field Company, PetroChina. The D_{max}-L data all come from publications: Elliott (1976), Scholz and Cowie (1990), Davis et al. (2005), Bergen and Shaw (2010), and Wei et al. (2020). They are listed in the references and cited in the text.

Declaration of competing interest

The authors declare that they have no known competing financial interests or personal relationships that could have appeared to influence the work reported in this paper.

Acknowledgments

This study received financial support from the National Key R&D Program of China (2021YFC3000604) and the National Natural Science Foundation of China (41872206). We thank the China Scholarship Council for their funding. We thank Petro China for providing proprietary seismic reflection profiles and drilling well data. We are grateful to Dr. Zhanyu Wei for providing the data and curves in Fig. 12. We express our deep appreciation to the editor, Prof. Jianhua Li, and the two anonymous reviewers for their valuable contributions to improving this manuscript.

Appendix A. Supplementary data

Supplementary data to this article can be found online at https://doi.org/10.1016/j.jsg.2025.105388.

References

Bailey, W.R., Walsh, J.J., Manzocchi, T., 2005. Fault populations, strain distribution and basement fault reactivation in the East Pennines Coalfield, UK. J. Struct. Geol. 27 (5), 913–928. https://doi.org/10.1016/j.jsg.2004.10.014.
Barnett, J.A., Mortimer, J., Rippon, J.H., Walsh, J.J., Watterson, J., 1987. Displacement geometry in the volume containing a single normal fault. AAPG (Am. Assoc. Pet. Geol.) Bull. 71 (8), 925–937. https://doi.org/10.1306/948878ED-1704-11D7-8645000102C1865D.
Baudon, C., Cartwright, J., 2008. The kinematics of reactivation of normal faults using high resolution throw mapping. J. Struct. Geol. 30 (8), 1072–1084. https://doi.org/10.1016/j.jsg.2008.04.008.
Bergen, K.J., Shaw, J.H., 2010. Displacement profiles and displacement-length scaling relationships of thrust faults constrained by seismic-reflection data. Bulletin 122 (7–8), 1209–1219. https://doi.org/10.1130/B26373.1.
Black, N.M., Jackson, D.D., 2008. Probability of multifault rupture. Bull. Seismol. Soc. Am. 98 (6), 3017–3024. https://doi.org/10.1785/0120070271.
Cartwright, J.A., Trudgill, B.D., Mansfield, C.S., 1995. Fault growth by segment linkage: an explanation for scatter in maximum displacement and trace length data from the Canyonlands Grabens of SE Utah. J. Struct. Geol. 17 (9), 1319–1326. https://doi.org/10.1016/0191-8141(95)00033-A.
Caumon, G., Collon-Drouaillet, P.L.C.D., Le Carlier de Veslud, C., Viseur, S., Sausse, J., 2009. Surface-based 3D modeling of geological structures. Math. Geosci. 41, 927–945. https://doi.org/10.1007/s11004-009-9244-2.
Chen, S.F., Deng, Q.D., Zhao, X.L., Wlison, C.J.L., Dirks, P., Luo, Z.L., Liu, S.G., 1994. Deformation characteristics, evolutionary history, and deformation mechanism of the middle longmenshan thrust-nappes and related tectonics. Seismol. Geol. 16 (4), 404–421. . (in Chinese).
Chen, Z.X., Jia, D., Zhang, Q., Wei, G.Q., Li, B.L., Wei, D.T., Shen, Y., 2005. Balanced cross-section analysis of the fold-thrust belt of the Longmen Mountains. Acta Geol. Sin. 79 (1), 38–45. . (in Chinese).
Chen, Z.X., Wang, L.N., Yang, G., Zhuang, B.J., Ying, D.L., Yuan, B.G., Pei, S.Q., Li, W., 2020. Geological structures and potential petroleum exploration areas in the southwestern Sichuan fold-thrust belt, SW China. Petrol. Explor. Dev. 47 (4), 699–713. https://doi.org/10.1016/S1876-3804(20)60086-6.
Childs, C., Holdsworth, R.E., Jackson, C.A.L., Manzocchi, T., Walsh, J.J., Yielding, G., 2017. Introduction to the geometry and growth of normal faults. Geolog. Soc. Lond. Special Pub. 439 (1), 1–9. https://doi.org/10.1144/SP439.24.
Childs, C., Nicol, A., Walsh, J.J., Watterson, J., 2003. The growth and propagation of synsedimentary faults. J. Struct. Geol. 25 (4), 633–648. https://doi.org/10.1016/S0191-8141(02)00054-8.
Childs, C., Watterson, J., Walsh, J.J., 1995. Fault overlap zones within developing normal fault systems. J. Geolog. So. London 152, 535–549. https://doi.org/10.1144/gsjgs.152.3.0535.
Cowie, P.A., Scholz, C.H., 1992a. Growth of faults by accumulation of seismic slip. J. Geophys. Res. 97, 11085e11096.
Cowie, P.A., Scholz, C.H., 1992b. Physical explanation for the displacement-length relationship of faults using a post-yield fracture mechanics model. J. Struct. Geol. 14 (10), 1133–1148. https://doi.org/10.1016/0191-8141(92)90065-5.
Cowie, P.A., Scholz, C.H., 1992c. Displacement-length scaling relationship for faults: data synthesis and discussion. J. Struct. Geol. 14 (10), 1149–1156. https://doi.org/10.1016/0191-8141(92)90066-6.
Davis, K., Burbank, D.W., Fisher, D., Wallace, S., Nobes, D., 2005. Thrust-fault growth and segment linkage in the active Ostler fault zone, New Zealand. J. Struct. Geol. 27 (8), 1528–1546. https://doi.org/10.1016/j.jsg.2005.04.011.
Dawers, N.H., Anders, M.H., 1995. Displacement-length scaling and fault linkage. J. Struct. Geol. 17 (5), 607–614. https://doi.org/10.1016/0191-8141(94)00091-D.
Dawers, N.H., Anders, M.H., Scholz, C.H., 1993. Growth of normal faults: displacement–length scaling. Geology 21 (12), 1107–1110. https://doi.org/10.1130/0091-7613(1993)021<1107:GONFDL>2.3.CO. . 2.
Deng, Q.D., Chen, S.F., Zhao, X.L., 1994. Tectonics, scismisity and dynamics of Longmenshan Mountains and its adjacent regions. Seismol. Geolog. 16 (4), 389–403. . (in Chinese).
Deng, Q.D., Wen, X.Z., 2008. A review on the research of active tectonics—history, Progress and Suggestions. Seismol. Geolog. 30 (1), 1–30. . (in Chinese).
DePolo, C.M., Clark, D.G., Slemmons, D.B., Ramelli, A.R., 1991. Historical surface faulting in the Basin and Range province, western North America: implications for fault segmentation. J. Struct. Geol. 13 (2), 123–136. https://doi.org/10.1016/0191-8141(91)90061-M.
Elliott, D., 1976. The energy balance and deformation mechanisms of thrust sheets. Phil. Trans. Roy. Soc. Lond. 283, 289–312.
Ellis, M.A., Dunlap, W.J., 1988. Displacement variation along thrust faults: implications for the development of large faults. J. Struct. Geol. 10 (2), 183–192. https://doi.org/10.1016/0191-8141(88)90115-0.
Ferrill, D.A., Morris, A.P., Wigginton, S.S., Smart, K.J., McGinnis, R.N., Lehrmann, D., 2016. Deciphering thrust fault nucleation and propagation and the importance of footwall synclines. J. Struct. Geol. 85 (apr), 1–11. https://doi.org/10.1016/j.jsg.2016.01.009.
Fossen, H., 2020. Fault classification, fault growth and displacement. In: Regional Geology and Tectonics. pp. 119–147. https://doi.org/10.1016/B978-0-444-64134-2.00007-9.
Fossen, H., Hesthammer, J., 1997. Geometric analysis and scaling relations of deformation bands in porous sandstone. J. Struct. Geol. 19 (12), 1479–1493. https://doi.org/10.1016/S0191-8141(97)00075-8.
Gillespie, P.A., Walsh, J.T., Watterson, J., 1992. Limitations of dimension and

displacement data from single faults and the consequences for data analysis and interpretation. J. Struct. Geol. 14 (10), 1157–1172. https://doi.org/10.1016/0191-8141(92)90067-7.

Guyonnet-Benaize, C., Lamarche, J., Hollender, F., Viseur, S., Münch, P., Borgomano, J., 2015. Three-dimensional structural modeling of an active fault zone based on complex outcrop and subsurface data: the Middle Durance Fault Zone inherited from polyphase Meso-Cenozoic tectonics (southeastern France). Tectonics 34 (2), 265–289. https://doi.org/10.1002/2014TC003749.

He, D.F., Li, D.S., Zhang, G.W., Zhao, L.Z., Fan, C., Lu, R.Q., Wen, Z., 2011. Formation and evolution of multi-cycle superposed Sichuan Basin, China. Chin. J. Geol. 46 (3), 589–606. . (in Chinese).

Henry, C., Das, S., 2001. Aftershock zones of large shallow earthquakes: fault dimensions, aftershock area expansion and scaling relations. Geophys. J. Int. 147 (2), 272–293.

Higgins, S., Clarke, B., Davies, R.J., Cartwright, J., 2009. Internal geometry and growth history of a thrust-related anticline in a deep water fold belt. J. Struct. Geol. 31 (12), 1597–1611.

Huang, W., Jiang, W.L., 2012. Discussion on the late quaternary activity and earthquake risk potential of longquanshan fault in sichuan. Northwest. Seismol. J. 34 (1), 50–56. . (in Chinese).

Hubbard, J., Shaw, J.H., Klinger, Y., 2010. Structural setting of the 2008 Mw 7.9 wenchuan, China, earthquake. Bull. Seismol. Soc. Am. 100 (5B), 2713–2735.

Jia, D., Li, Y.Q., Lin, A.M., Wang, M.M., Chen, W., Wu, X.J., Ren, Z.K., Zhao, Y., Luo, L., 2010. Structural model of 2008 Mw 7.9 Wenchuan earthquake in the rejuvenated Longmen Shan thrust belt, China. Tectonophysics 491 (1–4), 174–184. https://doi.org/10.1016/j.tecto.2009.08.040.

Jia, K., 2021. Modeling the spatiotemporal seismicity patterns of the Longmen Shan Fault Zone based on the Coulomb rate and state model. Seismol Res. Lett. 92 (1), 275–286. https://doi.org/10.1785/0220200088.

Kaneda, H., Nakata, T., Tsutsumi, H., Kondo, H., Sugito, N., Awata, Y., Akhtar, S.S., Majid, A., Khattak, W., Awan, A.A., Yeats, R.S., 2008. Surface rupture of the 2005 Kashmir, Pakistan, earthquake and its active tectonic implications. Bull. Seismol. Soc. Am. 98 (2), 521–557. https://doi.org/10.1785/0120070073.

Kase, Y., 2010. Slip-length scaling law for strike-slip multiple segment earthquakes based on dynamic rupture simulations. Bull. Seismol. Soc. Am. 100 (2), 473–481. https://doi.org/10.1785/0120090090.

Kim, Y.S., Sanderson, D.J., 2005. The relationship between displacement and length of faults: a review. Earth Sci. Rev. 68 (3–4), 317–334. https://doi.org/10.1016/j.earscirev.2004.06.003.

Kim, Y.S., Andrews, J.R., Sanderson, D.J., 2000. Damage zones around strike-slip fault systems and strike-slip fault evolution, Crackington Haven, southwest England. Geosci. J. 4 (2), 53–72. https://doi.org/10.1007/BF02910127.

Klinger, Y., 2010. Relation between continental strike-slip earthquake segmentation and thickness of the crust. J. Geophys. Res. Solid Earth 115 (B7). https://doi.org/10.1029/2009JB006550.

Lee, J.C., Chu, H.T., Angelier, J., Chan, Y.C., Hu, J.C., Lu, C.Y., Rau, R.J., 2002. Geometry and structure of northern surface ruptures of the 1999 Mw= 7.6 Chi-Chi Taiwan earthquake: influence from inherited fold belt structures. J. Struct. Geol. 24 (1), 173–192. https://doi.org/10.1016/S0191-8141(01)00056-6.

Lei, X.L., Su, J.R., Wang, Z.W., 2020. Growing seismicity in the Sichuan Basin and its association with industrial activities. Sci. China Earth Sci. 63, 1633–1660.

Lévy, B., Mallet, J.L., 1999. Discrete smooth interpolation: constrained discrete fairing for arbitrary meshes. ACM Trans. Graph. 8, 121–144.

Li, Z.G., Jia, D., Chen, W., 2013. Structural geometry and deformation mechanism of the Longquan anticline in the Longmen Shan fold-and-thrust belt, eastern Tibet. J. Asian Earth Sci. 64, 223–234. https://doi.org/10.1016/j.jseaes.2012.12.022.

Li, Z.G., Zhang, P.Z., Zheng, W.J., Jia, D., Hubbard, J., Almeida, R., Sun, C., Shi, X., Li, T., 2018. Oblique thrusting and strain partitioning in the Longmen Shan fold-and-Thrust Belt, eastern Tibetan plateau. J. Geophys. Res. Solid Earth 123 (5), 4431–4453. https://doi.org/10.1029/2018JB015529.

Li, Z.G., Zheng, W.J., Zhang, P.Z., Almeida, R., Jia, D., Sun, C., Wang, W.T., Li, T., 2019. Evidence for three Cenozoic phases of upper crustal shortening of the Xiongpo structure in the Longmen Shan fold-and-thrust belt, China: implications for the eastward growth of the eastern Tibetan Plateau. J. Asian Earth Sci. 179, 138–148. https://doi.org/10.1016/j.jseaes.2019.04.017.

Li, Z.W., Liu, S.G., Chen, H.D., Sun, D., Lin, J., Tang, C., 2011. Structural superimposition and conjunction and its effects on hydrocarbon accumulation in the Western Sichuan Depression. Petrol. Explor. Dev. 38 (5), 539–551. . (in Chinese).

Liu-Zeng, J., Zhang, Z., Wen, L., Tapponnier, P., Sun, J., Xing, X., Hu, G., Xu, Q., Zeng, L., Ding, L., Ji, C., Hudnut, K.W., Van der Woerd, J., 2009. Co-seismic ruptures of the 12 May 2008, Ms 8.0 Wenchuan earthquake, Sichuan: east–west crustal shortening on oblique, parallel thrusts along the eastern edge of Tibet. Earth Planet Sci. Lett. 286 (3–4), 355–370.

Liu, S.G., Li, Z.W., Cao, J.X., Liu, S., Deng, B., Wang, G.Z., Deng, B., 2009. 4-D textural and structural characteristics of Longmen intracontinental composite orogenic belt, southwest China. Chin. J. Geol. 44 (4), 1151–1180. . (in Chinese).

Liu, S.G., Luo, Z.L., Dai, S.L., Arne, D., Wilson, C.J.L., 1995. The uplift of the longmenshan thrust belt and subsidence of the western sichuan foreland basin. Acta Geol. Sin. 69 (3), 205–214. . (in Chinese).

Liu, S.G., Yang, Y., Deng, B., Zhong, Y., Wen, L., Sun, W., Li, Z.W., Jansa, L., Li, J.X., Song, J.M., Zhang, X.H., Peng, H.L., 2021. Tectonic evolution of the Sichuan Basin, southwest China. Earth Sci. Rev. 213, 103470.

Liu, S.M., Dixon, J.M., 1991. Centrifuge modelling of thrust faulting: structural variation along strike in fold-thrust belts. Tectonophysics 188 (1–2), 39–62.

Liu, Y., Tan, X., Ye, Y., Zhou, C., Lu, R., Murphy, M.A., Xu, X., Suppe, J., 2020. Role of erosion in creating thrust recesses in a critical-taper wedge: an example from Eastern Tibet. Earth Planet Sci. Lett. 540, 116270. https://doi.org/10.1016/j.epsl.2020.116270.

Lu, R.Q., He, D.F., John, S., Wu, J.E., Liu, B., Chen, Y.G., 2014. Structural model of the central Longmen Shan thrusts using seismic reflection profiles: implications for the sediments and deformations since the Mesozoic. Tectonophysics 630, 43–53.

Lu, R.Q., He, D.F., Suppe, J., Ma, X.M., Gui, B.L., Wang, M.J., Gao, J.W., 2010. The structures, formation and evolution of the shallow thrusting system in the central Longmen Mountains front belt. Chin. J. Geol. 45 (4), 997–1010. . (in Chinese).

Lu, R.Q., Xu, X.W., He, D.F., John, S., Liu, B., Wang, F.Y., Tan, X.B., Li, Y.Q., 2017. Seismotectonics of the 2013 lushan Mw 6.7 earthquake: inversion tectonics in the eastern margin of the Tibetan plateau. Geophys. Res. Lett. 44 (16), 8236–8243. https://doi.org/10.1002/2017GL074296.

Luo, Z.L., 1991. The dynamical model of the lithospheric evolution in Longmenshan orogenic belt. J. Chengdu Coll. Geol. 18 (1), 1–7. . (in Chinese).

Machette, M.N., Personius, S.F., Nelson, A.R., Schwartz, D.P., Lund, W.R., 1991. The Wasatch fault zone, Utah—segmentation and history of Holocene earthquakes. J. Struct. Geol. 13 (2), 137–149. https://doi.org/10.1016/0191-8141(91)90062-N.

Mallet, J.L., 1989. Discrete smooth interpolation. ACM Trans. Graph. 8 (2), 121–144. https://doi.org/10.1145/62054.62057.

Mallet, J.L., 1992. Discrete smooth interpolation in geometric modelling. Comput. Aided Des. 24 (4), 178–191. https://doi.org/10.1016/0010-4485(92)90054-E.

Manighetti, I., Campillo, M., Bouley, S., Cotton, F., 2007. Earthquake scaling, fault segmentation, and structural maturity. Earth Planet Sci. Lett. 253 (3–4), 429–438. https://doi.org/10.1016/j.epsl.2006.11.004.

Manighetti, I., Caulet, C., De Barros, L., Perrin, C., Cappa, F., Gaudemer, Y., 2015. Generic along-strike segmentation of A far normal faults, E ast A frica: implications on fault growth and stress heterogeneity on seismogenic fault planes. G-cubed 16 (2), 443–467. https://doi.org/10.1002/2014GC005691.

Manighetti, I., Zigone, D., Campillo, M., Cotton, F., 2009. Self-similarity of the largest-scale segmentation of the faults: implications for earthquake behavior. Earth Planet Sci. Lett. 288 (3–4), 370–381. https://doi.org/10.1016/j.epsl.2009.09.040.

Meyer, B., Tapponnier, P., Bourjot, L., Metivier, F., Gaudemer, Y., Peltzer, G., Guo, S.M., Chen, Z.T., 1998. Crustal thickening in Gansu-Qinghai, lithospheric mantle subduction, and oblique, strike-slip controlled growth of the Tibet plateau. Geophys. J. Int. 135 (1), 1–47.

Mildon, Z.K., Roberts, G.P., Faure Walker, J.P., Toda, S., 2019. Coulomb pre-stress and fault bends are ignored yet vital factors for earthquake triggering and hazard. Nat. Commun. 10 (1), 1–9. https://doi.org/10.1038/s41467-019-10520-6.

Mouslopoulou, V., Walsh, J.J., Nicol, A., 2009. Fault displacement rates on a range of timescales. Earth Planet Sci. Lett. 278 (3–4), 186–197. https://doi.org/10.1016/j.epsl.2008.11.031.

Nicol, A., Childs, C., Walsh, J.J., Manzocchi, T., Schöpfer, M.P.J., 2017. Interactions and growth of faults in an outcrop-scale system. Geolog. Soc. Lond. Special Pub. 439 (1), 23–39. https://doi.org/10.1144/SP439.9.

Nicol, A., Mouslopoulou, V., Begg, J., Oncken, O., 2020b. Displacement accumulation and sampling of paleoearthquakes on active normal faults of Crete in the eastern Mediterranean. G-cubed 21 (11), e2020GC009265. https://doi.org/10.1029/2020GC009265.

Nicol, A., Walsh, J.J., Villamor, P., Seebeck, H., Berryman, K.R., 2010. Normal fault interactions, paleoearthquakes and growth in an active rift. J. Struct. Geol. 32 (8), 1101–1113. https://doi.org/10.1016/j.jsg.2010.06.018.

Nicol, A., Walsh, J., Childs, C., Manzocchi, T., 2020a. The growth of faults. In: Understanding Faults. pp. 221–255.

Nicol, A., Watterson, J., Walsh, J.J., Childs, C., 1996. The shapes, major axis orientations and displacement patterns of fault surfaces. J. Struct. Geol. 18 (2–3), 235–248. https://doi.org/10.1016/S0191-8141(96)80047-2.

Nixon, C.W., Bull, J.M., Sanderson, D.J., 2014. Localized vs distributed deformation associated with the linkage history of an active normal fault, Whakatane Graben, New Zealand. J. Struct. Geol. 69, 266–280.

Oglesby, D.D., 2005. The dynamics of strike-slip step-overs with linking dip-slip faults. Bull. Seismol. Soc. Am. 95 (5), 1604–1622. https://doi.org/10.1785/0120050058.

Oglesby, D.D., 2008. Rupture termination and jump on parallel offset faults. Bull. Seismol. Soc. Am. 98 (1), 440–447. https://doi.org/10.1785/0120070163.

Peacock, D.C.P., 2002. Propagation, interaction and linkage in normal fault systems. Earth Sci. Rev. 58 (1–2), 121–142. https://doi.org/10.1016/S0012-8252(01)00085-X.

Peacock, D.C.P., Sanderson, D.J., 1991. Displacements, segment linkage and relay ramps in normal fault zones. J. Struct. Geol. 13 (6), 721–733. https://doi.org/10.1016/0191-8141(91)90033-F.

Peacock, D.C.P., Sanderson, D.J., 1996. Effects of propagation rate on displacement variations along faults. J. Struct. Geol. 18 (2–3), 311–320.

Poulimenos, G., 2000. Scaling properties of normal fault populations in the western Corinth Graben, Greece: implications for fault growth in large strain settings. J. Struct. Geol. 22 (3), 307–322. https://doi.org/10.1016/S0191-8141(99)00152-2.

Qian, Q., Han, Z.J., 2011. The research in the change of the earthquake occurrence probability in Longquan Shan fault after the Wenchuan earthquake. Prog. Geophys. 26 (2), 489–497. . (in Chinese).

Richardson, N.J., Densmore, A.L., Seward, D., Fowler, A., Wipf, M., Ellis, M.A., Li, Y., Zhang, Y., 2008. Extraordinary denudation in the Sichuan Basin: insights from low-temperature thermochronology adjacent to the eastern margin of the Tibetan Plateau. J. Geophys. Res. Solid Earth 113 (B4). https://doi.org/10.1029/2006JB004739.

Rippon, J.H., 1984. Contoured patterns of the throw and hade of normal faults in the Coal Measures (Westphalian) of north-east Derbyshire. Proc. Yorks. Geol. Soc. 45 (3), 147–161. https://doi.org/10.1144/pygs.45.3.147.

Ross, Z.E., Cochran, E.S., Trugman, D.T., Smith, J.D., 2020. 3D fault architecture controls the dynamism of earthquake swarms. Science 368 (6497), 1357–1361. https://doi.org/10.1126/science.abb0779.

Rotevatn, A., Jackson, C.A., Tvedt, A.B.M., Bell, R., Blækkan, I., 2019. How do normal faults grow? J. Struct. Geol. 125, 174–184. https://doi.org/10.1016/j.jsg.2018.08.005.

Schlagenhauf, A., Manighetti, I., Malavieille, J., Dominguez, S., 2008. Incremental growth of normal faults: insights from a laser-equipped analog experiment. Earth Planet Sci. Lett. 273 (3–4), 299–311. https://doi.org/10.1016/j.epsl.2008.06.042.

Schlische, R.W., Young, S.S., Ackermann, R.V., Gupta, A., 1996. Geometry and scaling relations of a population of very small rift-related normal faults. Geology 24 (8), 683–686. https://doi.org/10.1130/0091-7613(1996)024<0683:GASROA>2.3.CO. . 2.

Scholz, C.H., Cowie, P.A., 1990. Determination of geologic strain from fault slip data. Nature 346, 837–839.

Scholz, C.H., Dawers, N.H., Yu, J.Z., Anders, M.H., Cowie, P.A., 1993. Fault growth and fault scaling laws: preliminary results. J. Geophys. Res. Solid Earth 98 (B12), 21951–21961. https://doi.org/10.1029/93JB01008.

Schultz, R.A., Soliva, R., Fossen, H., Okubo, C.H., Reeves, D.M., 2008. Dependence of displacement-length scaling relations for fractures and deformation bands on the volumetric changes across them. J. Struct. Geol. 30, 1405e1411.

Schwartz, D.P., Coppersmith, K.J., 1984. Fault behavior and characteristic earthquakes: examples from the Wasatch and San Andreas fault zones. J. Geophys. Res. Solid Earth 89 (B7), 5681–5698. https://doi.org/10.1029/JB089iB07p05681.

Shaw, B.E., Dieterich, J.H., 2007. Probabilities for jumping fault segment stepovers. Geophys. Res. Lett. 34 (1). https://doi.org/10.1029/2006GL027980.

Shaw, J.H., Connors, C., Suppe, J., 2005. Seismic Interpretation of Contractional Fault-Related Folds. The American Association of Petroleum Geologists, Tulsa, Oklahoma, U.S.A.

Soliva, R., Benedicto, A., 2004. A linkage criterion for segmented normal faults. J. Struct. Geol. 26 (12), 2251–2267. https://doi.org/10.1016/j.jsg.2004.06.008.

Song, G.H., Wang, M.M., Jiang, D.Q., Chen, Z.X., Yan, B., Feng, W., 2019. Along-strike structural linkage and interaction in an active thrust fault system: a case study from the western Sichuan foreland basin, China. Basin Res. 33 (1), 210–226. https://doi.org/10.1111/bre.12461.

Su, G.P., Li, Z.Q., Ying, D.L., Li, G., Ying, W.F., Yang, Y.Y., Liu, H.L., Ding, X., Tang, H.Q., 2020. Formation and evolution of the Caledonian paleo-uplift and itsgenetic mechanism in the Sichuan Basin. Acta Geol. Sin. 94 (6), 1793–1812.

Suppe, J., 1983. Geometry and kinematics of fault-bend folding. Am. J. Sci. 283 (7), 684–721.

Tang, L.J., Yang, K.M., Jin, W.Z., Lü, Z.Z., Yu, Y.X., 2008. Multi-level decollement zones and detachment deformation of Longmenshan thrust belt, Sichuan Basin, southwest China. Sci. China Earth Sci. 51 (2), 32–43. https://doi.org/10.1007/s11430-008-6014-9.

Tapponnier, P., Molnar, P., 1977. Active faulting and tectonics in China. J. Geophys. Res. 82 (20), 2905–2930.

Tapponnier, P., Xu, Z.Q., Roger, F., Meyer, B., Arnaud, N., Wittlinger, G., Yang, J.S., 2001. Oblique stepwise rise and growth of the Tibet Plateau. Science 294 (5547), 1671–1677.

Totake, Y., Butler, R.W., Bond, C.E., Aziz, A., 2018. Analyzing structural variations along strike in a deep-water thrust belt. J. Struct. Geol. 108, 213–229.

Walsh, J.J., Watterson, J., 1988. Analysis of the relationship between displacements and dimensions of faults. J. Struct. Geol. 10 (3), 239–247. https://doi.org/10.1016/0191-8141(88)90057-0.

Walsh, J.J., Bailey, W.R., Childs, C., Nicol, A., Bonson, C.G., 2003. Formation of segmented normal faults: a 3-D perspective. J. Struct. Geol. 25 (8), 1251–1262. https://doi.org/10.1016/S0191-8141(02)00161-X.

Walsh, J.J., Nicol, A., Childs, C., 2002. An alternative model for the growth of faults. J. Struct. Geol. 24 (11), 1669–1675. https://doi.org/10.1016/S0191-8141(01)00165-1.

Wang, C.S., Dai, J.G., Zhao, X.X., Li, Y.L., Graham, S.A., He, D.F., Ran, B., Meng, J., 2014. Outward-growth of the Tibetan plateau during the cenozoic: a review. Tectonophysics 621, 1–43. https://doi.org/10.1016/j.tecto.2014.01.036.

Wang, J.Y., Lu, R.Q., Zhang, H., Li, J.H., Li, L.M., Xu, H.G., Gu, Q.P., Shu, P., Hou, Y., 2020. Three-dimensional geological modeling of Cenozoic erathem in Jiangsu segment of the Tanlu fault zone. Acta Geol. Sin. 42 (2), 216–230. . (in Chinese).

Wang, M.M., Hubbard, J., Plesch, A., Shaw, J.H., Wang, L.N., 2016. Three-dimensional seismic velocity structure in the Sichuan basin, China. J. Geophys. Res. Solid Earth 121 (2), 1007–1022. https://doi.org/10.1002/2015JB012644.

Wang, S.Y., Liu, K.Y., Wang, H.X., Chen, M.Y., 2022. Growth and linkage of normal faults experiencing multiple non-coaxial extension: a case from the Qikou Sag, Bohai Bay Basin, East China. Basin Res. 34 (2), 748–770. https://doi.org/10.1111/bre.12639.

Wang, W.T., Jia, D., Li, C.Y., Zheng, W.J., Wei, Z.Y., 2008. Preliminary investigation on deformation characteristics and activity of longquanshan fault belt in sichuan. Seismol. Geol. 30 (4), 968–979. . (in Chinese).

Watterson, J., 1986. Fault dimensions, displacements and growth. Pure Appl. Geophys. 124 (1), 365–373. https://doi.org/10.1007/BF00875732.

Wei, Z.Y., He, H.L., Sun, W., Zhuang, Q.T., Liang, Z.H., 2020. Investigating thrust-fault growth and segment linkage using displacement distribution analysis in the active Duzhanzi thrust fault zone, Northern Tian Shan of China. J. Struct. Geol. 133, 103990. https://doi.org/10.1016/j.jsg.2020.103990.

Wells, D. L., Coppersmith, K. J., 1994. New empirical relationships among magnitude, rupture length, rupture width, rupture area, and surface displacement. Bulletin of the seismological Society of America 84 (4), 974–1002.

Wesnousky, S.G., 2006. Predicting the endpoints of earthquake ruptures. Nature 444 (7117), 358–360. https://doi.org/10.1038/nature05275.

Willemse, E.J., 1997. Segmented normal faults: correspondence between three-dimensional mechanical models and field data. J. Geophys. Res. Solid Earth 102 (B1), 675–692.

Willemse, E.J.M., Pollard, D.D., Aydin, A., 1996. 3D analyses of slip distributions on normal fault arrays with consequences for fault scaling. J. Struct. Geol. 18 (2–3), 295–309.

Wilson, J.E., Chester, J.S., Chester, F.M., 2003. Microfracture analysis of fault growth and wear processes, Punchbowl Fault, San Andreas system, California. J. Struct. Geol. 25 (11), 1855–1873. https://doi.org/10.1016/S0191-8141(03)00036-1.

Wojtal, S.F., 1994. Fault scaling laws and the temporal evolution of fault systems. J. Struct. Geol. 16 (4), 603–612. https://doi.org/10.1016/0191-8141(94)90100-7.

Xu, F., Lu, R.Q., Wang, S., Jiang, G.Y., Long, F., Wang, X.S., Su, P., Liu, G.S., 2022. Study on the seismotectonics of the Qingbaijiang Ms 5.1 earthquake in Sichuan Province in 2020 by multiple constraint method. Seismol. Geol. 44 (1), 220–237. . (in Chinese).

Xu, S.S., Nieto-Samaniego, A.F., Alaniz-Álvarez, S.A., Velasquillo-Martinez, L.G., 2006a. Effect of sampling and linkage on fault length and length–displacement relationship. Int. J. Earth Sci. 95 (5), 841–853. https://doi.org/10.1007/s00531-005-0065-3.

Xu, S.S., Ren, H., Song, J., 2006b. Primary study on the seismicity along the faults of Longquanshan. Earthquake Res. Sichuan 2, 21–27. . (in Chinese).

Xu, X.W., Wen, X.Z., Yu, G.H., Chen, G.H., Klinger, Y., Hubbard, J., Shaw, J., 2009. Coseismic reverse-and oblique-slip surface faulting generated by the 2008 Mw 7.9 Wenchuan earthquake, China. Geology. 37 (6), 515–518.

Yan, D.P., Zhou, M.F., Li, S.B., Wei, G.Q., 2011. Structural and geochronological constraints on the Mesozoic-Cenozoic tectonic evolution of the Longmen Shan thrust belt, eastern Tibetan Plateau. Tectonics 30 (6). https://doi.org/10.1029/2011TC002867.

Yue, L.F., Suppe, J., Hung, J.H., 2005. Structural geology of a classic thrust belt earthquake: the 1999 Chi-Chi earthquake Taiwan (Mw = 7.6). J. Struct. Geol. 27, 2058–2083. https://doi.org/10.1016/j.jsg.2005.05.020.

Yu, G.H., Xu, X.W., Klinger, Y., Diao, G.L., Chen, G.H., Feng, X.D., Li, C., Zhu, A., Yuan, R., Guo, T., Sun, X., 2010. Fault-scarp features and cascading-rupture model for the Mw 7.9 wenchuan earthquake, eastern Tibetan plateau, China. Bull. Seismol. Soc. Am. 100 (5B), 2590–2614. https://doi.org/10.1785/0120090255.

Ze, T., Alves, T.M., 2016. The role of gravitational collapse in controlling the evolution of crestal fault systems (Espírito Santo Basin, SE Brazil). J. Struct. Geol. 92, 79–98. https://doi.org/10.1016/j.jsg.2016.09.011.

Ze, T., Alves, T.M., 2017. The role of gravitational collapse in controlling the evolution of crestal fault systems (Espírito Santo Basin, SE Brazil)-Reply. J. Struct. Geol. 98, 12–14. https://doi.org/10.1016/j.jsg.2017.03.005.

Zhang, P.Z., Mao, F.Y., Slemmons, D.B., 1999. Rupture terminations and size of segment boundaries from historical earthquake ruptures in the Basin and Range Province. Tectonophysics 308 (1–2), 37–52. https://doi.org/10.1016/S0040-1951(99)00089-X.

Zhang, P., Slemmons, D.B., Mao, F.Y., 1991. Geometric pattern, rupture termination and fault segmentation of the Dixie Valley—pleasant Valley active normal fault system, Nevada, USA. J. Struct. Geol. 13 (2), 165–176. https://doi.org/10.1016/0191-8141(91)90064-P.

Leonard, M., 2010. Earthquake fault scaling: Self-consistent relating of rupture length, width, average displacement, and moment release. Bulletin of the Seismological Society of America, 100(5A), 1971-1988.